Numerical Simulation of the Generation of Airfoil Tones at a Moderate Reynolds Number

Christopher K.W. Tam[*] and Hongbin Ju[†]
Florida State University, Tallahassee, Florida, 32306-4510, USA

Experimentally, it is known that an airfoil with a round trailing edge operating at a moderate Reynolds number emits tones. The objective of this work is to investigate the tone generation mechanisms by direct numerical simulation. At low angle of attack, the wake flow of the airfoil is quite symmetric about the flow direction. The tone intensity is relatively low. It is found that the wake flow is highly unstable. A tone is generated as a by-product of the generation of Kelvin-Helmholtz instability wave. The tone frequency is the same as that of the most amplified wave. At high angle of attack, a separation bubble forms at the leading edge of the airfoil. The flow is dominated by vortices. The emitted tone is intense. Observations reveal that wake vortices are shed in pairs. The pressure inside a vortex is low but between vortex pairs the pressure is high. Pressure fluctuations are created in the high- and low-pressure regions of the row of vortices when they adjust their relative position to accommodate the shedding of a new pair of vortices. These pressure fluctuations are the sources of sound. It is important to point out that the sound source is not highly localized. Details of the sound generation processes are reported in this paper.

I. Introduction

IN recent years, there has been a good deal of interest in the aeroacoustic community to compute the flow around airfoil[1–3] and the associated sound[4–10]. These investigations are made possible by rapid advances in computational methodology, turbulence modeling and in the availability of fast parallel computers. For high Reynolds number flows, the method of choice is Large Eddy Simulation (LES). This is the method used in Refs. 1 and 3. This same approach is also used for computing the noise radiated from airfoils[4–10]. Since high spatial resolution is required for turbulence and high frequency sound computations, the computational domains used by many investigators are inevitably small. This presents a special challenge in computing noise radiation to the far field. In Refs.4 to 10, there is no attempt to do a direct computation to the far field. Invariably, a hybrid method is used to extend the numerical solution in a limited domain to the far acoustic field. For this purpose, the use of the Acoustic Analogy method is most popular. However, attempts have been made to use the Ffowcs-Williams and Hawkings method or the Kirchoff Integral representation. Chang *et al.*[11] performed similar numerical simulations but with an emphasis on the effect of vortex shedding. Lummer *et al.*[12] investigated the influence of trailing edge geometry of an airfoil on sound generation. Despite tremendous advance in LES, it is still not a method for practical application at the present time. For instance, to make practical estimate of wind turbine noise[13–15] or helicopter rotor noise[16] semi-empirical methods are used. Aside from computational studies, there are also a number of experimental investigators[17–19] on airfoil noise. However, the emphasis of these experimental works is not the same as the computational investigations.

Small wind turbines are generally operated at moderate Reynolds number. It is known experimentally that airfoils with blunt trailing edge in the Reynolds number range of $5 \times 10^4 < R_c < 3 \times 10^5$ generate distinct tones. Here R_c is based on chord width. Figure 1 shows the noise spectra of three small airfoils tested in this range of Reynolds number[20]. The noise spectra are clearly dominated by tones. The objective of this project is to investigate the tone generation mechanisms by numerical simulations. One advantage of numerical simulation is that the entire set of space-time data is available. This allows detailed study and analysis of different tone generation mechanisms. A complete set of data is difficult to measure experimentally. Within the Reynolds number range considered, the Reynolds number based on the boundary layer displacement thickness at the trailing edge, R_{δ^*}, for small airfoils, is

[*] Robert O. Lawton Distinguished Professor, Department of Mathematics, Fellow AIAA.
[†] Research Associate, Department of Mathematics, Senior Member AIAA.

less than 1,000. At these moderate Reynolds numbers, the flow could remain laminar all the way to the far wake, provided the levels of free stream turbulence and sound intensity are low. This is the case in the present numerical simulation study.

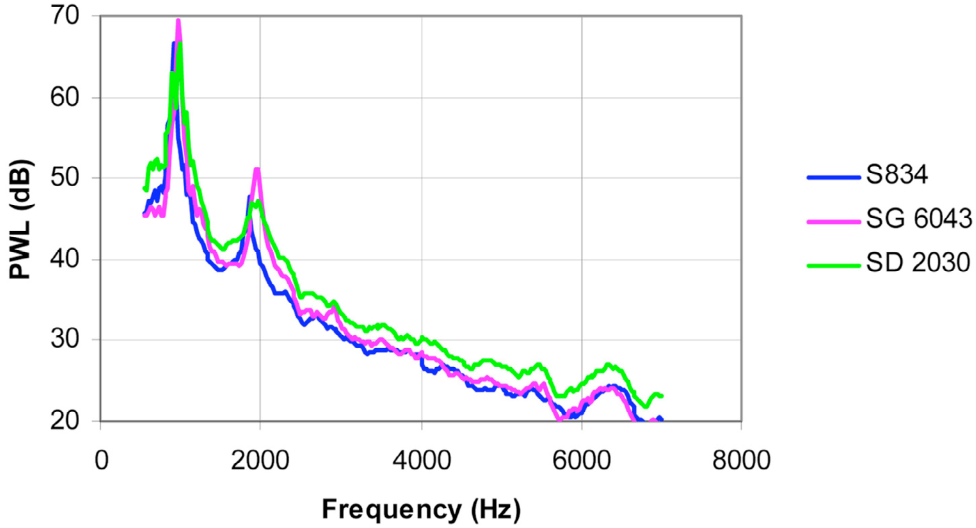

Fig. 1. Noise spectra of three small airfoils at flow velocity of 22.4 m/s. Angle of attack is 10^0 for S834, 0^0 for SG 6043 and SD 2030 airfoils. Data from Oerlemans[20].

The flow around an airfoil may be categorized into four regimes depending on the angle of attack. They are:

1. Low angle of attack with symmetric or nearly symmetric wake flow.
2. Moderate angle of attack with unsymmetric wake flow.
3. High angle of attack with leading edge separation bubble.
4. Very high angle of attack with open separation flow.

For wind turbine application, the wind direction could vary significantly over a relatively short period of time. It has been reported that separated flow occurs at some part of a wind turbine most of the time[21]. Thus all four categories of flow are possible for small wind turbines.

In this investigation, numerical simulations of the flow and acoustic field of an NACA0012 airfoil with a blunt trailing edge at $R_c = 2 \times 10^5$ are carried out. Results at low and high angles of attack will be reported in this paper. Results at moderate and very high angles of attack will be reported in a subsequent paper. Although the observed characteristics of the tones emitted by the airfoil including intensities, directivity and waveforms will be reported here, they are not the main focus of this work. Of utmost importance to this investigation are the mechanisms by which tones are generated. Evidence will be presented to show that at low angle of attack tone generation is closely related to the generation of instability waves in the wake flow. It is believed that the tones are generated as a by-product of the generation of Kelvin-Helmholtz instability in the wake of the airfoil. At high angle of attack, strong vortex pairs are shed from the airfoil. In the vicinity of the trailing edge of the airfoil, the vortices are dynamically locked together through mutual influence. The adjustment of these vortices to the induced field of each other, as new vortices roll past the trailing edge on the suction side of the airfoil and are shed, leads to the formation of localized instantaneous high and low pressure regions. Pressure fluctuations in these regions are the sources of the tones.

The rest of this paper is as follows. In Section II, the computational model used in the present study is presented. A conformal mapping method for the development of body fitted grids for airfoils as well as the computation algorithm are described. Sections III and IV report the observations and results of numerical simulations of an airfoil at low and high angle of attack, respectively. The noise intensity, directivity and spectrum are presented in Section V. Section VI concludes this work.

II. Computational Model, Grid Design and Algorithm

A. Computational Model

In this study, the computational model consists of a NACA0012 airfoil with a rounded trailing edge. The chord width, C, is $0.1m$. The airfoil is placed in a uniform stream with a velocity, u_∞, of 29 m/s. Since the kinematic viscosity of air, ν, at 15° C is 0.145×10^{-4} m²/s, the Reynolds number of the model is 2×10^5. For a flat plate with the same length, the displacement thickness at the trailing edge is $\delta^* = 1.72(\nu C/u_\infty)^{1/2} = 3.85 \times 10^{-4}$ m. Thus, R_{δ^*} is equal to 770. For this Reynolds number, the wake flow is still laminar in the absence of high levels of ambient turbulence.

The governing equations are the dimensionless Navier-Stokes equations in two dimensions and the energy equation. Here the length scale is C (chord width), velocity scale is a_∞ (ambient sound speed), time scale is C/a_∞, density scale is ρ_∞ (ambient gas density), pressure and stress scales are $\rho_\infty a_\infty^2$. These equations are,

$$\frac{\partial \rho}{\partial t} + \rho \frac{\partial u_j}{\partial x_j} + u_j \frac{\partial \rho}{\partial x_j} = 0 \tag{1}$$

$$\frac{\partial u_i}{\partial t} + u_j \frac{\partial u_i}{\partial x_j} = -\frac{1}{\rho}\frac{\partial p}{\partial x_i} + \frac{1}{\rho}\frac{\partial \tau_{ij}}{\partial x_j} \tag{2}$$

$$\frac{\partial p}{\partial t} + u_j \frac{\partial p}{\partial x_j} + \gamma p \left(\frac{\partial u_j}{\partial x_j}\right) = 0 \tag{3}$$

where
$$\tau_{ij} = \frac{M}{R_c}\left(\frac{\partial u_i}{\partial x_j} + \frac{\partial u_j}{\partial x_i}\right); \qquad R_c = \frac{C u_\infty}{\nu}\ ; \qquad M = \frac{u_\infty}{a_\infty} \tag{4}$$

u_∞ is the free stream velocity, $M = u_\infty/a_\infty$ is the Mach number. R_c is the Reynolds number based on chord width. Both viscous dissipation and heat conduction are neglected in the energy equation.

B. Grid Design

A well-designed grid is crucial to an accurate numerical simulation. For flow past an airfoil, accurate resolution of the boundary layer and wake flow is very important. To be able to do so, the use of a body fitted grid is most desirable.

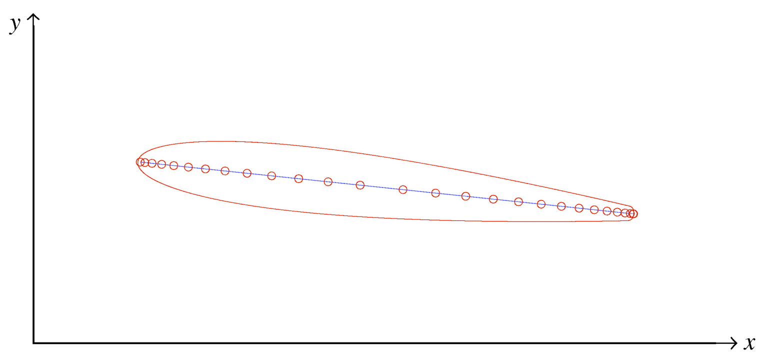

Fig. 2a. Source distribution along the camber line of an airfoil.

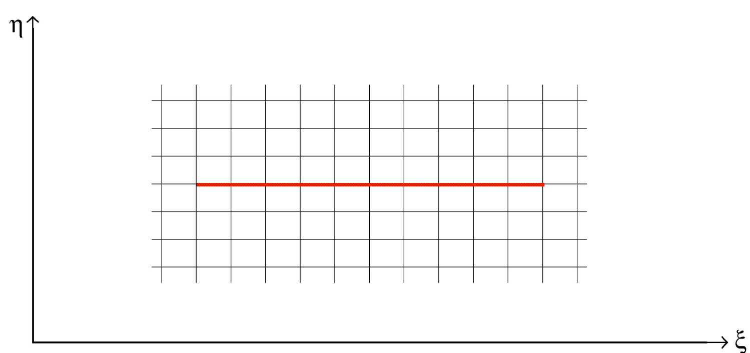

Fig. 2b. Mapping of the airfoil into a slit in the w-plane.

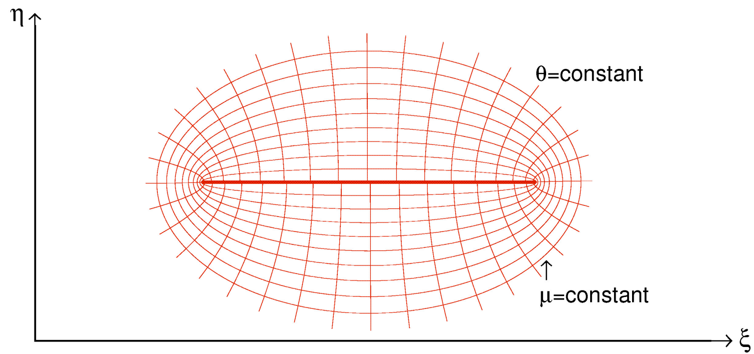

Fig. 2c. Elliptic coordinates around the slit as body fitted grid for the airfoil.

As a part of this investigation, a method to generate a very accurate body fitted grid for arbitrary airfoil geometry has been developed. The method consists of two essential steps as schematically illustrated in Fig. 2. The first step is a mapping of the airfoil in the physical x–y-plane into a slit in the w or the ξ–η-plane. This is accomplished by conformal transformation using a multitude of point sources distributed along the camber line of the airfoil as shown in Fig. 2a. The appropriate form of the conformal transformation is,

$$w = z + \sum_{j=1}^{N} Q_j \log\left(\frac{z - z_j}{z - z_0}\right) + i\gamma \tag{5}$$

where w = $\xi + i\eta$ is the complex coordinates of a point in the mapped plane. $z = x + iy$ is a point in the physical plane. Q_j, z_j (j = 1,2,…,N) are the source strengths and locations. γ is just a constant. The inclusion of γ in the mapping function is important. Its inclusion makes it possible to map the airfoil onto a slit on the real axis of the w-plane (see Fig. 2b). z_0 is the location of a reference source. A good location to place z_0 is in the middle of the camber line such that all the lines joining z_j to z_0 lie within the airfoil. In this way, the branch cuts associated with the log functions of Eq. (5) would not present a problem in the computation.

In implementing the mapping, the coordinates z_j (j = 1,2,3,…,N) of the source points are first assigned. A useful rule in assigning the source locations is that the distance $| z_j - z_{j-1} |$ should be in some way proportional to the local thickness of the airfoil. That is to say, the sources should be closer together at where the airfoil is thin. Now the source strengths Q_j (j = 1,2,…,N) are to be chosen to accomplish the mapping. For this purpose, a set of points, z_k (k = 1,2,…,M) around the surface of the airfoil is chosen to enforce the mapping. z_k are the enforcement points. M should be much larger than N. On imposing the conditions that the surface of the airfoil be mapped onto a slit on the real axis of the w-plane on Eq. (5) leads to the following system of linear equation for Q_j and γ.

$$y_k + \sum_{j=1}^{N} \mathrm{Im}\left[Q_j \log\left(\frac{z_k - z_j}{z_k - z_0}\right)\right] + \gamma = 0\,, \qquad k = 1,2,\ldots,M\,. \tag{6}$$

This system of equations may be written in a matrix form,

$$\mathbf{Ax} = \mathbf{b} \tag{7}$$

where $\mathbf{x}$ is a column vector of length $(2N + 1)$. The elements of $\mathbf{x}$ are

$$x_{2j-1} = \mathrm{Re}(Q_j)\,, \quad x_{2j} = \mathrm{Im}(Q_j), \qquad j = 1,2,\ldots,N$$
$$x_{2N+1} = \gamma$$

$\mathbf{A}$ is a $M \times (2N + 1)$ matrix. The elements of $\mathbf{A}$ are,

$$a_{i,2j} + i a_{i,2j\square 1} = \log \square \frac{z_i \square z_j}{z_i \square z_0} \square$$

$$a_{i,2N+1} = 1, \qquad i = 1,2,\ldots,M; \quad j = 1,2,3,\ldots,N$$

b is a column vector of length M. The elements of **b** are

$$b_k = \square y_k, \qquad k = 1,2,3,\ldots,M.$$

With $M >> 2N+1$ Equation (7) is an over-determined system. A least squares solution may be obtained by first premultiplying Eq. (7) by the transpose of **A**. This leads to the normal equation

$$\mathbf{A}^{\mathrm{T}}\mathbf{A}\mathbf{x} = \mathbf{A}^{\mathrm{T}}\,\mathbf{b}, \tag{8}$$

which can be easily solved by any standard matrix solver.

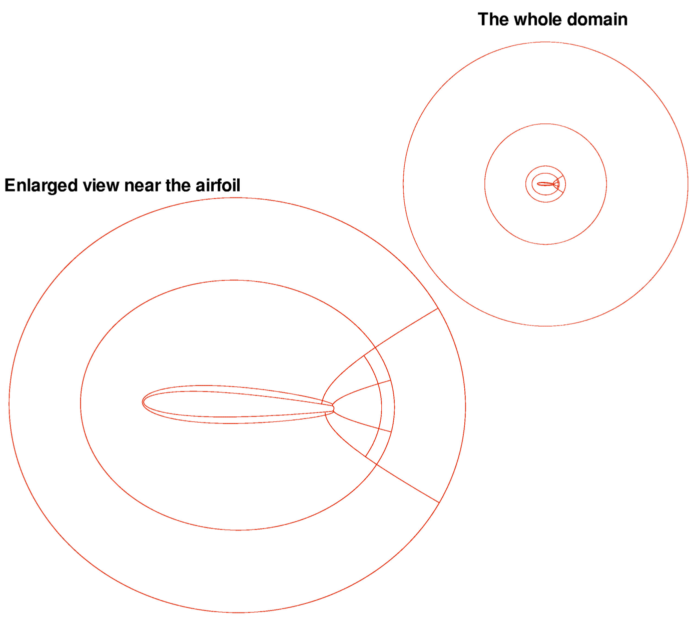

Fig. 3. The various subdomains of a multi-size mesh in the elliptic coordinates region of the computational domain.

The second step in developing a body fitted grid to the airfoil is to take the mid-point of the slit in the $\square$–$\square$-plane as the center of an elliptic coordinate system. Let the width of the slit be a and $\bar{\square}$ be the $\square$ coordinate measured from the mid-point of the slit. The elliptic coordinates ($\square$,$\square$) are related to ($\bar{\square}$,$\square$) by

$$\bar{\square} = \frac{a}{2}\cosh\square\cos\square, \qquad \square = \frac{a}{2}\sinh\square\sin\square. \tag{9}$$

The elliptic coordinate system is shown in Fig. 2c. The elliptic coordinate system is orthogonal. The curve $\square = 0$ is the surface of the airfoil in the physical plane. The boundary layer lies in the region $\square < \square$ in the $\square$–$\square$-plane. The wake is in the region $-\square_1 < \square < \square_2$ where $\square$, $\square_1$ and $\square_2$ are small quantities. In the present simulations, these are the regions with the finest meshes.

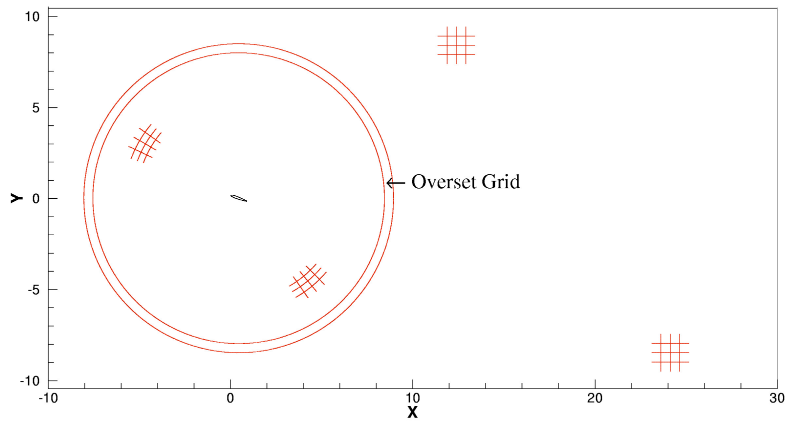

Fig. 4. The computational domain showing the elliptic coordinates region, the Cartesian coordinates region and the overset grid.

The problem at hand is a multi-scales problem. The smallest length scale of the problem that needs to be resolved is in the viscous boundary layer and in the wake. In this work, a multi-size mesh is used in the time marching computation. Figure 3 shows the boundaries of the different mesh size blocks in the elliptical coordinates region of the computation domain. The mesh size increases by a factor of 2 as one crosses a mesh-size-change boundary going outward from the airfoil. For large η, the elliptical coordinates become circular. At a radius of about 8 chord width, the computation switches from the $\xi - \eta$ coordinates to a rectangular Cartesian coordinates in the physical plane as shown in Fig. 4. The Cartesian mesh extends to 30 chord downstream from the airfoil. It is 10 chords wide on both top and bottom sides of the airfoil. The reason to use such a large computational domain is to provide sufficient distance for the wake and shed vortices to fully develop and to decay before exiting the computational boundary.

C. Computational Algorithm

For time marching computation in the elliptic coordinates region of the computational domain, Eqs. (1) to (4) are first rewritten in the $\xi - \eta$ coordinates. The derivatives are then discretized according to the 7-point stencil Dispersion-Relation-Preserving (DRP) scheme[22]. At the mesh-size-change boundaries, the multi-size-mesh multi-time-step DRP scheme[23] is implemented. This scheme allows the smooth connection and transfer of the computed results using two different size meshes on the two sides of the boundary. Another important feature of this method is that it also allows a change in the size of the time step. This makes it possible to maintain numerical stability without being forced to use very small time steps in sub-domains where the mesh size is large. This makes the computation efficient without loss of accuracy.

In the nearly circular region of the computation domain (see Fig. 4), the computation is carried out in the $\xi - \eta$-plane. Outside this region, a rectangular mesh is used. The computation is performed in the x–y-plane. At the overlapping boundary of these two regions, overset grids method[24] is used to transfer data from one set of grid to the other set. The data transfer process is accomplished by the use of a sixteen-point optimized interpolation stencil. The interpolation process has a comparable accuracy as the time marching computation scheme.

Near the airfoil surface where backward difference stencils are used, artificial selective damping[25] is introduced to damp out spurious waves and grid-to-grid oscillations created by the presence of the wall (a discontinuity). In addition, general background artificial selective damping terms are added to all discretized governing equations. This ensures the removal of any residual spurious waves that might exist in the computational domain.

On the left, the top and bottom boundaries of the computational domain shown in Fig. 4, radiation boundary conditions[22] are imposed. On the right side of the boundary, outflow boundary conditions given in Ref. 22 are enforced. On the airfoil surface, the $u = v = 0$ no-slip boundary conditions are imposed. This, however, will create an over-determined system of equations if all the discretized governing equations are required to be satisfied at the boundary points. To avoid this problem, the two momentum equations of the Navier-Stokes equations are not enforced at the wall boundary points. The continuity and energy equations are, nevertheless, computed to provide the values of density, ρ, and pressure, p, at the airfoil surface.

To start the computation, the variables are set equal to the values of the uniform flow, namely, u = M, $v = 0$, $\rho = 1$ and $p = 1/\gamma$. The solution is then time marched until it is deemed periodic. At high angle of attack, the numerical solution exhibits some small elements of chaotic behavior. This prevents the solution from attaining an exactly periodic state. In this case, numerical data are measured when a quasi-periodic state is achieved.

III. Airfoil at 2 Degrees Angle of Attack

We will consider an airfoil at 2 degrees angle of attack as typical of airfoils at low angle of attack. The results and observations of our numerical simulation are described below.

A. Mean Flow and Vorticity Field

At low angle of attack, the wake flow exhibits near symmetry. Figure 5 shows the mean velocity profiles at four stations downstream of the airfoils. The profiles are nearly perfectly symmetric. The velocity deficit evolves quickly into a Gaussian shape. The wake flow is highly unsteady. Figure 6 shows an instantaneous vorticity field associated with the flow past the airfoil. The lines in the figure are constant vorticity contours. Beyond approximately two chord widths downstream of the trailing edge, well-defined vortices are formed. Further downstream, the vortices align in a staggered pattern. The direction of rotation for the vortices above the centerline of the wake is clockwise. Those below the centerline rotate in a counter-clockwise direction. The strength of the vortices decreases as they are convected further and further downstream. Figure 7 is an enlarged picture of Fig. 6 concentrating on the near wake. It should be clear from this figure that there are distributed vorticity throughout the boundary layer and in the near wake. There is no shedding of vortices at the trailing edge of the airfoil. The wake starts to oscillate up and down just downstream of the airfoil trailing edge. The intensity of oscillation increases as the flow moves downstream. The oscillations attain a significant amplitude at about 0.2 chord distance. Beyond this location the vorticity in the wake starts to organize into discrete isolated vortices. Eventually the vortex system resembles a Karman vortex street.

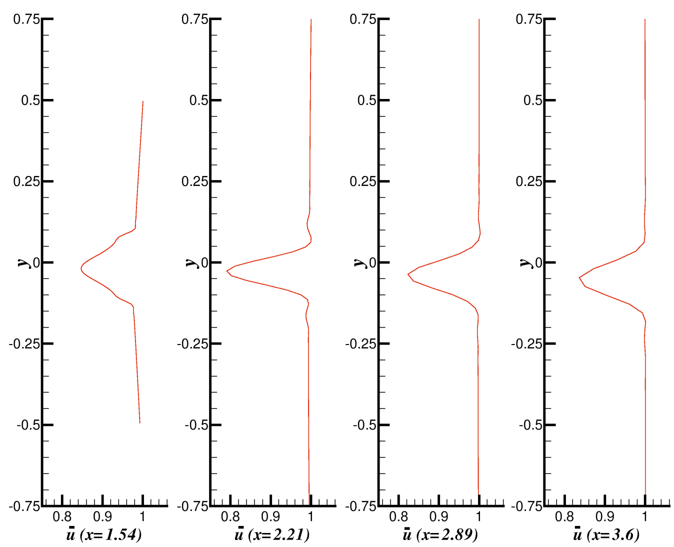

Fig. 5. Mean velocity profiles measured from numerical simulation data at four stations in the wake of a NACA0012 airfoil at 2 degrees angle of attack.

Further information about the flow can be found in the instantaneous streamline pattern of the wake. Figure 8 is the streamline pattern of the wake flow from the numerical simulation. It shows clearly the oscillatory motion of the wake with the highest amplitude at around 0.2 chord distance from the trailing edge. The oscillation has a well-defined wavelength. This figure strongly suggests that the wake is unstable. The oscillatory motion is driven by the Kelvin-Helmholtz instability. The Kelvin-Helmholtz instability has a large growth rate. After being excited near the trailing edge, the instability grows quickly to attain a maximum amplitude at a distance around 0.2C downstream. The instability wave is responsible for organizing the vorticity in the wake flow into discrete vortices as shown in Figs. 6 and 7. To demonstrate that the oscillations of the wake is due to Kelvin-Helmholtz instability, it will be shown below that the wavelength of oscillation (Fig. 8) is equal to that of the most amplified instability wave. Further, the root-mean-squared pressure fluctuation distributions in the wake match the instability eigenfunctions reasonably well.

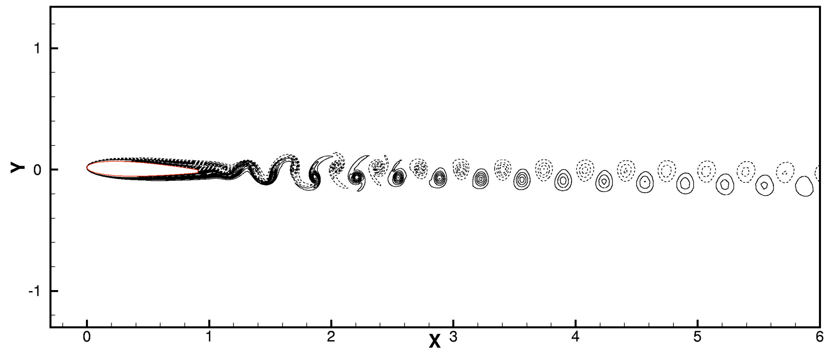

Fig. 6. Instantaneous vorticity contour plot of the flow past a NACA0012 airfoil at 2 degrees angle of attack.

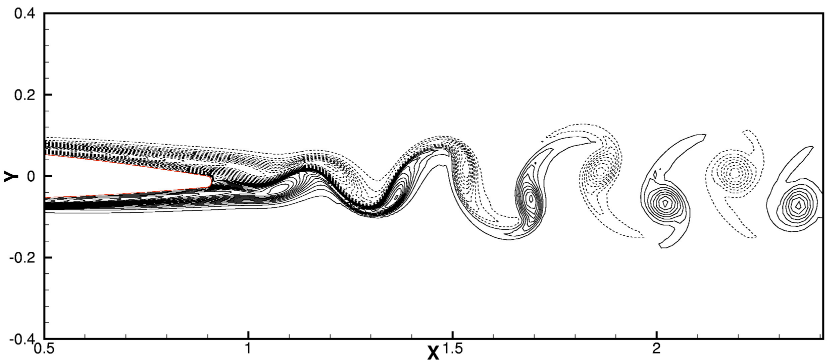

Fig. 7. Instantaneous vorticity contours in the near wake of a NACA0012 airfoil at 2 degrees angle of attack.

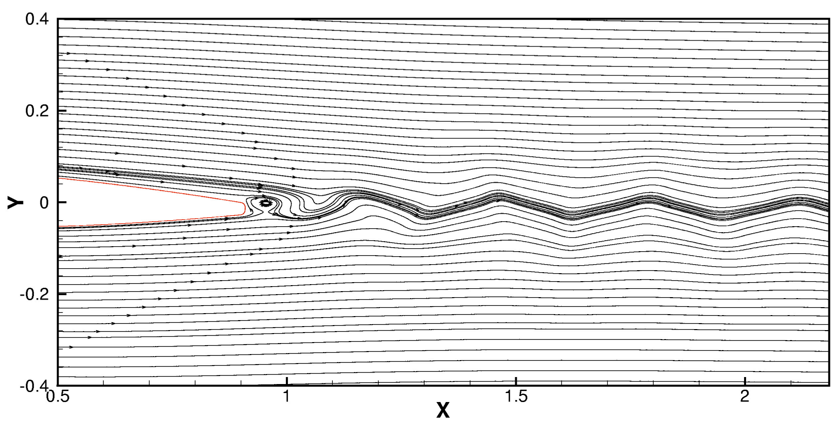

Fig. 8. Instantaneous streamline pattern of the wake of a NACA0012 airfoil at 2 degrees angle of attack.

B. Kelvin-Helmholtz Instability

Kelvin-Helmholtz instability is an inflexional instability for which viscosity is unimportant. For the present purpose, a linear inviscid analysis would be sufficient. By decomposing the flow variables into a mean and a time fluctuating part and on assuming locally parallel flow, the time dependent component of the flow are governed by the linearized Euler and energy equations. In dimensionless form, using u_∞ (the free stream velocity) as the velocity scale (instead of a_∞ as in previous section) and C/u_∞ as time scale, ρu^2 as the pressure scale, these equations are,

$$\bar{\rho}\left(\frac{\partial u}{\partial t} + \bar{u}\frac{\partial u}{\partial x} + v\frac{d\bar{u}}{dy}\right) = -\frac{\partial p}{\partial x} \tag{10}$$

$$\bar{\rho}\left(\frac{\partial v}{\partial t} + \bar{u}\frac{\partial v}{\partial x}\right) = -\frac{\partial p}{\partial y} \tag{11}$$

$$\frac{\partial p}{\partial t} + \bar{u}\frac{\partial p}{\partial x} + \frac{1}{M^2}\left(\frac{\partial u}{\partial x} + \frac{\partial v}{\partial y}\right) = 0. \tag{12}$$

In the above equations, quantities with a bar are mean flow quantities. On following the normal mode approach, wave-like solutions of the form,

$$\begin{bmatrix} u \\ v \\ p \end{bmatrix} = \mathrm{Re}\left\{ \begin{bmatrix} \hat{u}(y) \\ \hat{v}(y) \\ \hat{p}(y) \end{bmatrix} e^{i(kx-\omega t)} \right\} \tag{13}$$

are sought. On substituting Eq. (13) into Eqs. (10) to (12) and by eliminating $\hat{u}$, the governing equations reduce to a coupled set of ordinary differential equations,

$$\frac{d\hat{p}}{dy} = i\bar{\rho}(\omega - \bar{u}k)\hat{v} \tag{14}$$

$$\frac{d\hat{v}}{dy} = \left[iM^2(\omega - \bar{u}k) - \frac{ik^2}{\bar{\rho}(\omega - \bar{u}k)}\right]\hat{p} - \frac{k\frac{d\bar{u}}{dy}}{(\omega - \bar{u}k)}\hat{v}. \tag{15}$$

For large y, $\bar{u} \to 1$, $\bar{\rho} \to 1$, the solution of Eqs. (14) and (15) that is bounded as $y \to \infty$ is

$$\hat{p} = Ae^{-[k^2 - M^2(\omega - k)^2]^{1/2} y} \tag{16}$$

$$\hat{v} = A\frac{i\left[k^2 - M^2(\omega - k)^2\right]^{\frac{1}{2}}}{(\omega - k)} e^{-[k^2 - M^2(\omega - k)^2]^{1/2} y}. \tag{17}$$

Now, the boundary conditions at $y = 0$ are,

$$\text{Symmetric modes,} \qquad \frac{d\hat{p}}{dy} = 0 \quad \text{or} \quad \hat{v} = 0 \tag{18}$$

$$\text{Antisymmetric modes,} \qquad \hat{p} = 0 \quad \text{or} \quad \frac{d\hat{v}}{dy} = 0. \tag{19}$$

Solutions of Eqs. (14) and (15), which behave like Eqs. (16) and (17) for large y and at the same time satisfy boundary condition Eqs. (18) and (19) are eigensolutions. For a given ω, k is the eigenvalue. The eigenvalue is complex ($k = k_r + ik_i$). The spatial growth rate is equal to $-k_i$. The eigenvalue problem can be readily solved computationally by using Eqs. (16) and (17) as the starting solution (ω given, k is a trial value) and integrating the solution from a large value of y to $y = 0$. k is then adjusted by the Newton's iteration until the boundary condition at $y = 0$ is satisfied. Here k is the dimensionless wave number. It is related to the wavelength λ by $k_r = 2\pi/\lambda$. For the measured mean velocity profiles of Fig. 5, the calculated k_r for the most amplified wave (antisymmetric mode) is $k_{\text{average}} = 19.41$. The measured value from the simulation data is $k_{\text{average}} = 19.94$. The good agreement provides strong support that the wake oscillation of Fig. 8 and the vortex train of Fig. 6 are the results of Kelvin-Helmholtz instability in the wake flow.

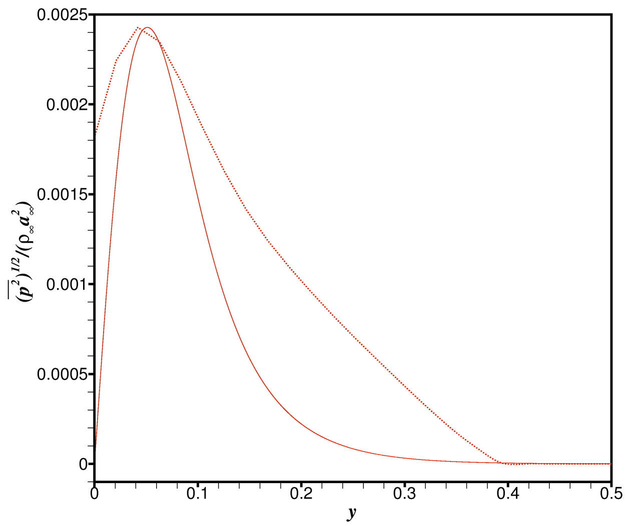

Fig. 9. Comparison between measured root-mean-squared pressure fluctuations in the wake of a NACA 0012 airfoil at 2 degrees angle of attack and eigenfunction of wake instability at $x/C = 2.89$. ——— instability theory, · · · · · · · numerical simulation.

As further confirmation of wake instability, the pressure eigenfunction at different downstream stations are computed. Figure 9 shows a comparison of the pressure eigenfunction and the measured root-mean-squared pressure fluctuations at $x = 2.89$. Figure 10 shows a similar comparison at $x = 3.6$. It is evident that the simulation has a small component of the symmetric instability wave mode superimposed on the most amplified antisymmetric mode. On taking this into consideration, the agreements are reasonably good.

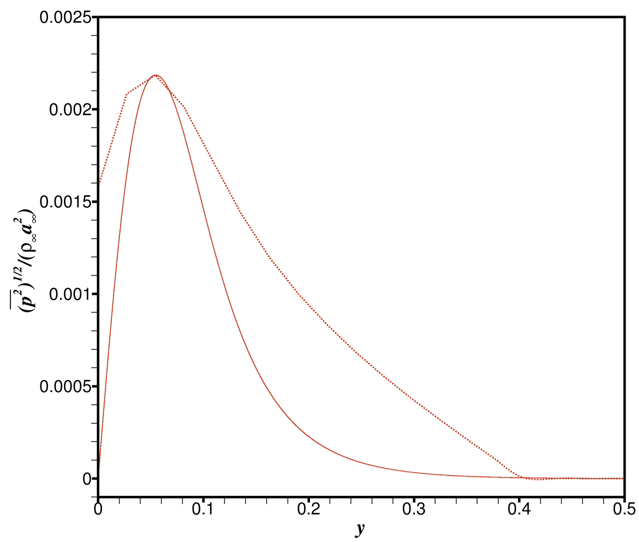

Fig. 10. Comparison between measured root-mean-squared pressure fluctuations in the wake of a NACA 0012 airfoil at 2 degrees angle of attack and eigenfunction of wake instability at $x/C = 3.6$. ——— instability theory, · · · · · · · numerical simulation.

C. Observation of the Sound Generation Processes

The present numerical simulation confirms the general belief that the unsteady wake flow of the airfoil is responsible for the emission of a tone near the trailing edge. Now we will investigate the details of the tone generation processes. To facilitate this effort, the contours of density fluctuation, $\square$, defined by,

$$\rho' = \rho - \bar{\rho} \tag{20}$$

where $\bar{\rho}$ is the time average of ρ, are computed. For low Mach number flows, p' is directly related to ρ'. Of special interest to us is the $r' = 0$ or the zero density contour. We will use this contour as an indicator of the acoustic wave front. We will track the propagation of this contour from just outside the wake flow to the far field.

Figure 11 is a sequence of ρ' contour distributions computed over a half period of wake oscillation. Figure 11a is typical of the distribution of ρ' when the next pulse of acoustic wave is about to be emitted. In this figure, the $\rho' = 0$ contours extend from regions inside the wake flow to the outside. For clarity, we have added a symbol (+) to indicate a region where ρ' is positive and a symbol (–) to indicate a region where ρ' is negative. In Fig. 11a, the background region on the top half of the figure is a (–) region, while the background region in the lower half is a (+) region. Notice that the first major (+) and (–) lobe extending outside the wake comes from the regions of the wake at approximately 0.2*C* downstream from the airfoil trailing edge. Also the contour distribution pattern is nearly symmetrical about the centerline of the wakes except that the sign of ρ' above is exactly opposite to that below. Thus, if a positive pressure pulse is emitted to the upper half of the computational domain a similar negative pulse is simultaneously emitted to the bottom half. Figure 11b shows the ρ' distribution at a slightly later time. Clearly, at this time, the first 3 main (+) and (–) lobes have expanded outward. Figure 11c, at a still later time, shows the coalescing of the zero ρ' contours from the first three lobes on the top to form a single front. The same happens on the bottom at a moment later. Figures 11d and 11e, at even later times, indicate how the two wave fronts, one marking the spread of a positive pressure pulse and the other a negative pressure pulse, propagate from the source region in the wake to the far field away from the airfoil. At the completion of a half cycle, the sequence repeats itself except with the (+) and (–) regions interchanged.

On examining the ρ' contours it is found that the highest and lowest value occur periodically and nearly simultaneously at around a region about 0.2 chord distance downstream of the trailing edge of the airfoil. As mentioned above, this is the region from which the first main lobe of the $\rho' = 0$ contour extends outside the wake. Thus, these highest and lowest pressure regions are major sources of sound. Recall that this is the region where wake oscillations or Kelvin-Helmholtz instability are excited. Based on the above observations, it is our contention that the airfoil tone is generated as a by-product of the generation of Kelvin-Helmholtz instability in the wake flow. The acoustic energy is but a tiny fraction of the instability wave energy. One important point we would like to emphasize is that the source of sound is not localized at a point. It is spread out in space. In other words, it is not really a compact source. Also, it is not located right at the trailing edge of the airfoil.

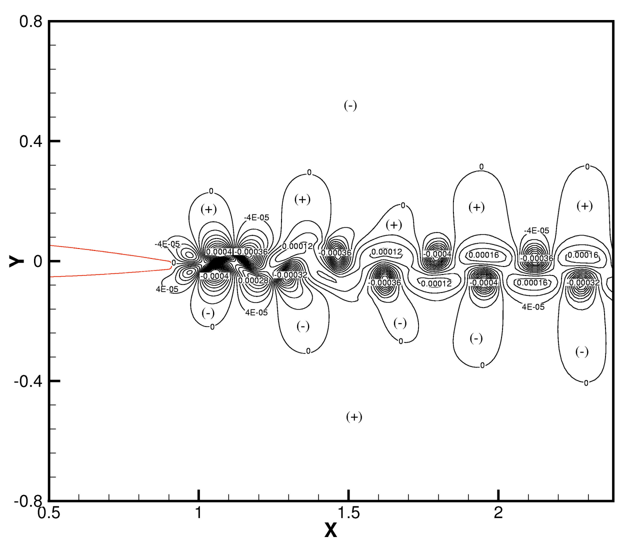

Fig. 11a. The ρ' contour pattern of a NACA0012 airfoil at 2 degrees angle of attack at five instants of time. (+) high density and high pressure region, (–) low density and low pressure region.

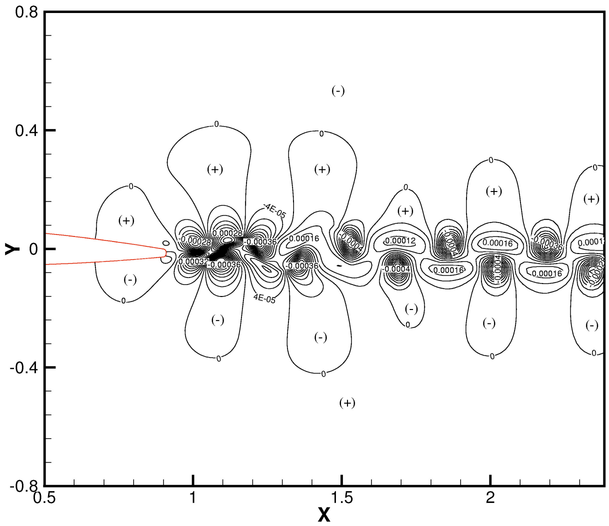

Fig. 11b.

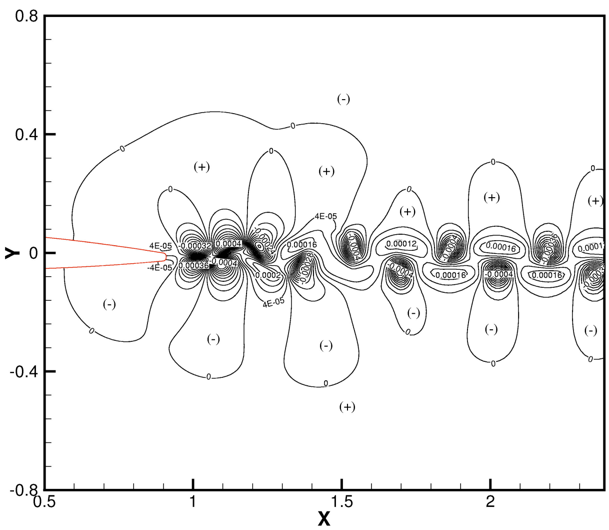

Fig. 11c.

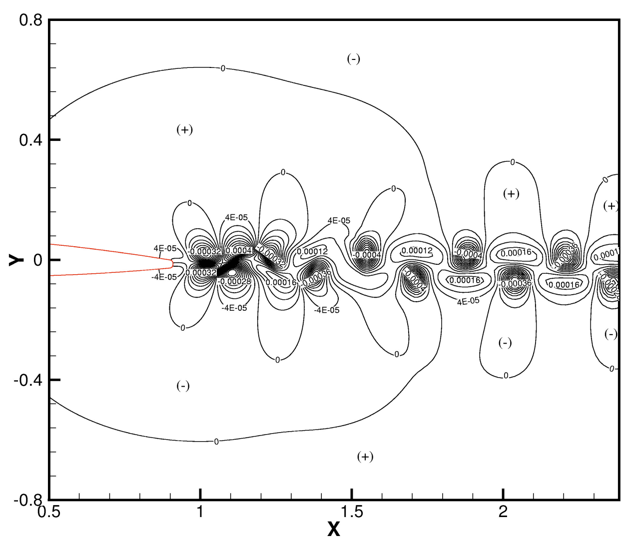

Fig. 11d

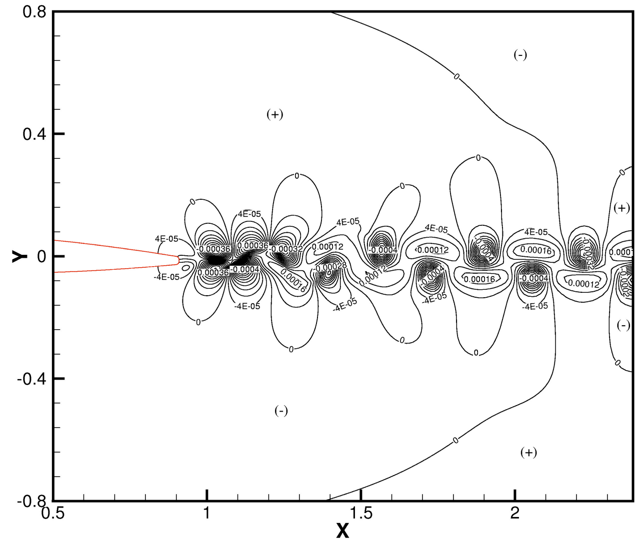

Fig. 11e.

IV. Airfoil at 8 Degrees Angle of Attack

At high angle of attack, say at 8 degrees, the flow field around the airfoil as well as the tone generation processes are very different from that at low angle of attack. In this section, we will first discuss the mean and unsteady flow especially in the wake region. Then observations on the tone generation processes are reported.

A. Mean and Unsteady Flow Around the Airfoil

The mean flow profiles in the wake of the airfoil at 8 degrees angle of attack are shown in Fig. 12. They are measured at the same stations as Fig. 5. It is easy to see that the mean flow profiles are vastly different from those at low angle of attack. The profiles are quite irregular. At high angle of attack, the wake flow contains many large vortices. As a result, it is extremely unsteady. For such highly unsteady flow, it is possible that the mean flow is not at any time close to a real realization of the actual flow. Thus, the mean flow may not be a very meaningful quantity to characterize the actual state of the flow.

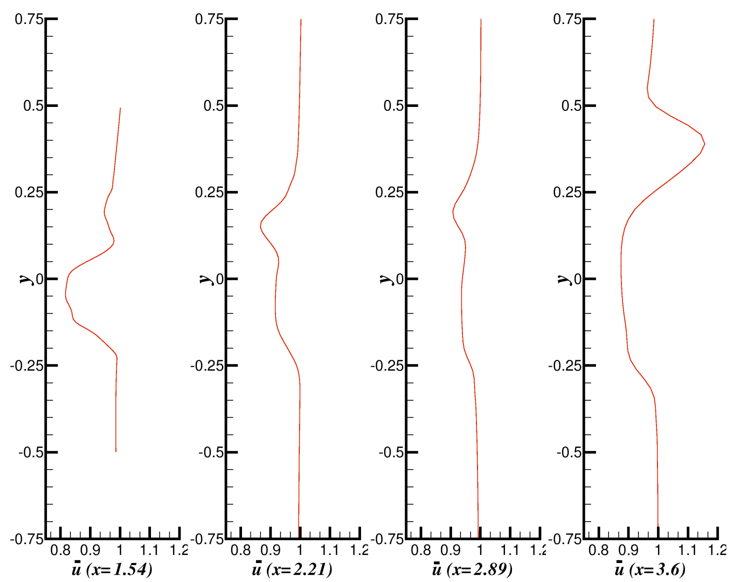

Fig. 12. Mean velocity profiles measured from numerical simulation data at four stations in the wake of a NACA0012 airfoil at 8 degrees angle of attack.

A more useful way to look at the flow associated with a NACA0012 airfoil with a rounded trailing edge at 8 degrees angle of attack is to examine the vorticity field. Figure 13 shows the vorticity field at an instance in the numerical simulation. The flow separates at the leading edge and reattaches at about 1/3 chord on the suction side of the airfoil. The detached flow is highly unstable. The unstable Kelvin-Helmholtz instability waves roll up quickly into a large vortex. This vortex moves down the suction side of the airfoil. It exerts a good deal of influence on the dynamics of the flow. Figure 13 reveals that the wake consists of two vortex systems. There is a row of vortex pairs on the top-side of the wake. The vortex pairs are carried downstream by the external flow as well as by their mutual induced velocity. A row of weak vorticity is formed on the bottom side of the wake. These vortices dissipate rapidly beyond three chord distance downstream of the trailing edge of the airfoil. It is believed that these vortices play only a minor role in the overall dynamics of the wake flow.

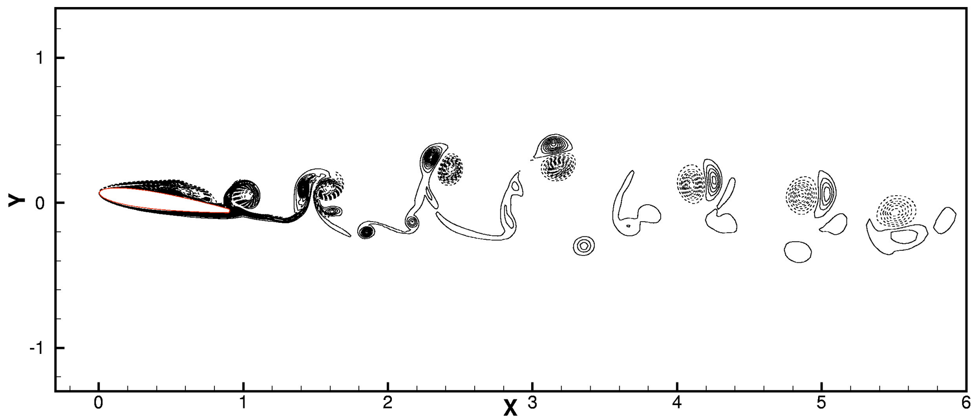

Fig. 13. Instantaneous vorticity contour plot of the flow past a NACA0012 airfoil at 8 degrees angle of attack.

Of great importance to sound generation is the process by which vortices are shed from the airfoil. This process is best observed by following the changes in the spatial distribution of the vorticity of the flow. This is illustrated in the sequence of vorticity contour plots of Fig. 14. Figure 14a shows a large vortex that originates from the leading edge separated flow is about to shed from the trailing edge of the airfoil. This vortex has a clockwise rotation. Figure 14b, at a short time later, indicates that as the large vortex moves half way past the trailing edge, its large clockwise rotating flow induces a counter-clockwise flow of fluid from the pressure side of the airfoil. This counter-clockwise flow rolls up quickly into a large vortex as shown in Fig. 14c. At a short time later, the clockwise and counter-clockwise vortices form a pair and break loose from the airfoil. This is illustrated in Fig. 14d. As the vortex pair breaks away from the trailing edge of the airfoil, the boundary layer from the pressure side of the airfoil continues to feed fluid into the counter-clockwise rotating vortex. Because the vortices are moving away in the downstream direction the boundary layer fluid shed from the pressure side of the airfoil is stretched into a thin shear layer. This is best seen in Fig. 14e. This thin shear layer containing a significant amount of vorticity is unstable. At a later time, the vorticity concentrates into a well-defined single vortex. This process might have been instigated by the intrinsic instability of the shear layer flow.

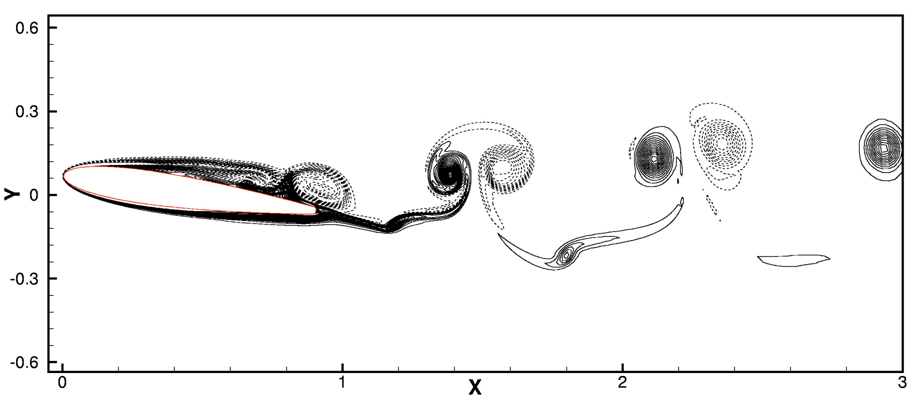

Fig. 14a. Vorticity contour plots of the near wake of a NACA0012 airfoil at 8 degrees angle of attack at five instants of time showing the shedding of vortex pairs from the trailing edge.

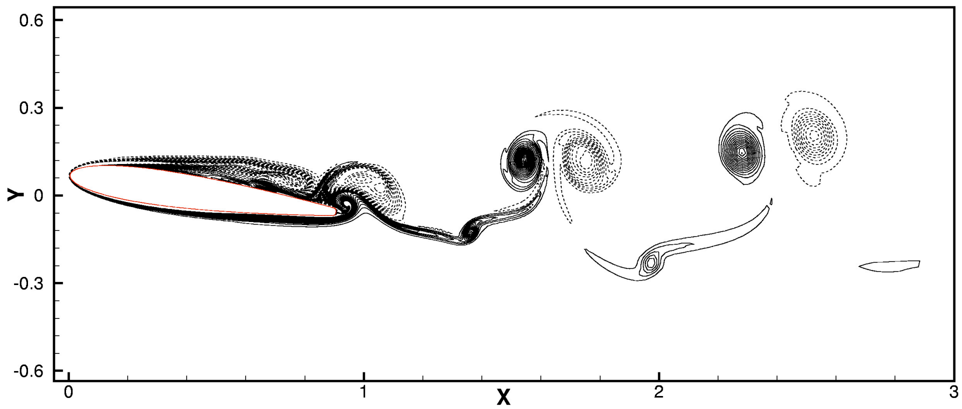

Fig. 14b.

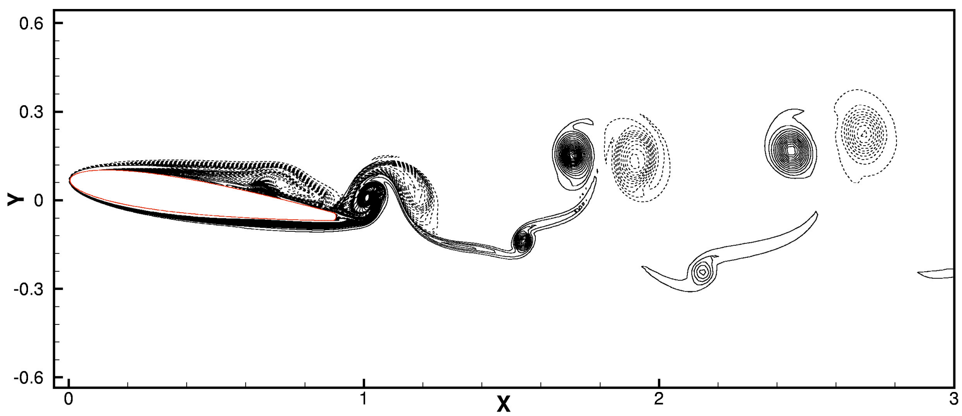

Fig. 14c.

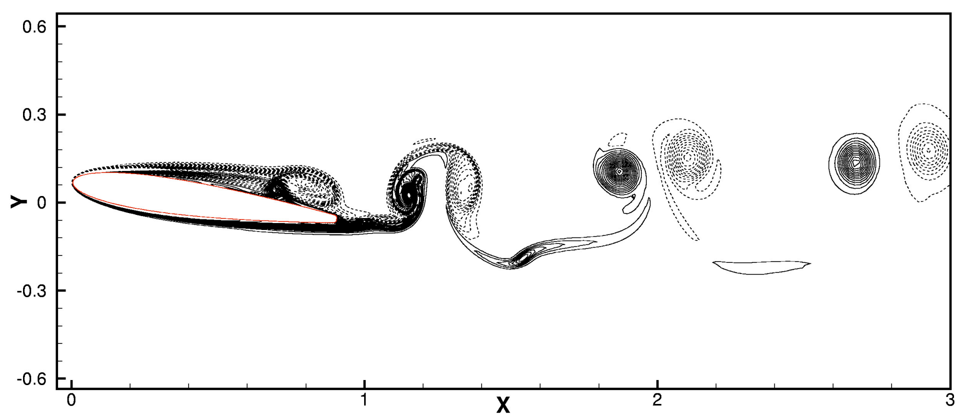

Fig. 14d.

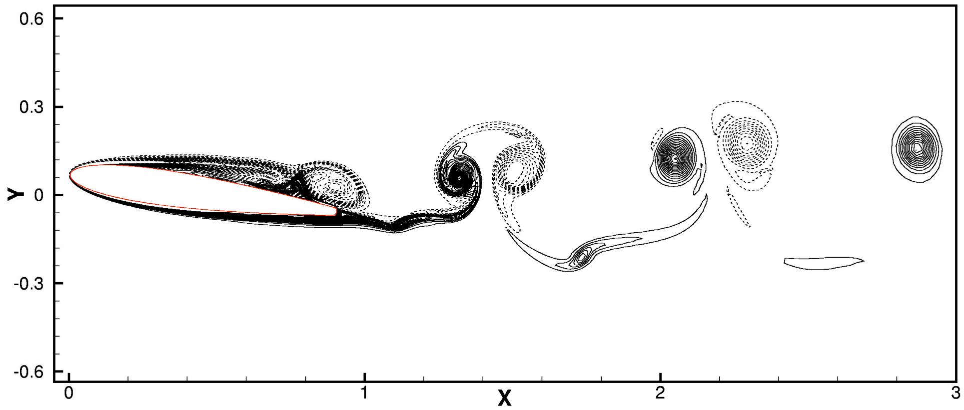

Fig. 14e.

It is relevant to point out another feature of the vortices of Fig. 14. In Fig. 14a, just upstream of the large vortex that is about to move off the airfoil trailing edge is a smaller clockwise rotating vortex. This vortex grows in strength by absorbing vorticity from the leading edge separation bubble. In between the two vortices, on the suction side of the airfoil, is a nearly stagnation region created by the opposing flow of the two neighboring vortices. Because of the high-speed flow inside a vortex, the pressure and density are low in the core region. In the stagnation region, however, the flow velocity is low. Thus, it builds up into a high-pressure region. It is, therefore, useful to note that on the suction side of the airfoil there is a high-pressure region sandwiched between two vortices with low pressure cores.

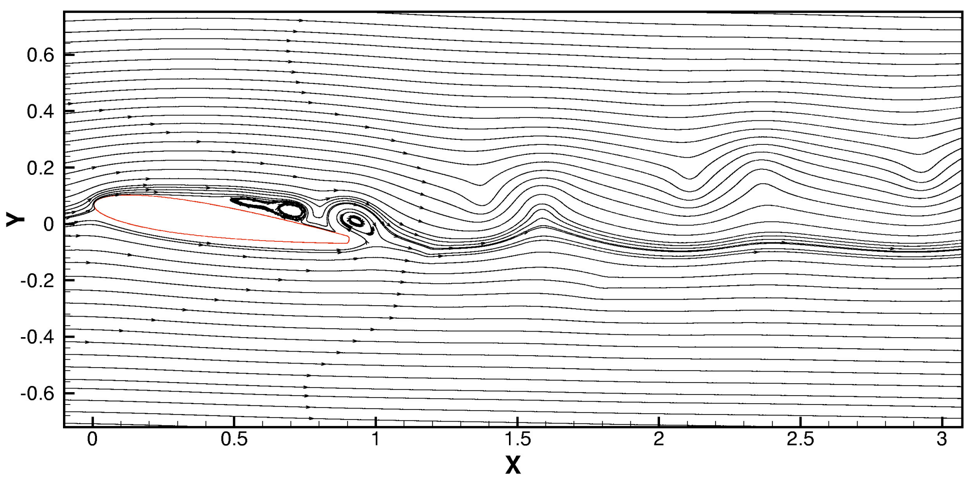

Fig. 15. Instantaneous stream line pattern of the wake of a NACA0012 airfoil at 8 degrees angle of attack.

Figure 15 shows the streamline pattern of the flow around the airfoil at an instant. The existence of two vortices on the suction side of the airfoil can clearly be seen. The large oscillations in the streamline pattern is caused by the large vortices in the wake flow. The location of each large wake vortex is marked by a localized shape bend of the streamline pattern. It is interesting to compare Fig. 15 with Fig. 8, the streamline pattern at low angle of attack. The large differences in the streamline pattern are indications of the almost total change in the dynamics of the two flows.

B. Sound Generation Processes

We will now use the pressure fluctuation contours or the p' contours to investigate the acoustic sources and radiation processes of the airfoil at 8 degrees angle of attack. p' is defined by,

$$p' = p - \bar{p}\,. \tag{21}$$

Specifically, we will use the $p' = 0$ contour as an indicator of the wave front, as we have done before.

Figure 16 shows the changes in the spatial distribution of the p' contours during half a cycle. For this half cycle, the background pressure fluctuation in the upper half plane is negative and that in the lower half plane is positive. Figure 16a shows the four positive pressure lobes extending outside the wake flow in the top half pane. At the same time, there are three negative pressure lobes in the lower half plane. Downstream of the trailing edge of the airfoil, high pressure regions are formed between vortex pairs. On the suction side of the airfoil, the stagnation region between the two clockwise rotating vortices is also a high-pressure region. This was mentioned before. As a large vortex is shed from the airfoil trailing edge, the motion apparently causes a slight decrease in the spacing between the shed vortex and the first vortex pair in the wake flow leading to an increase in pressure. This same motion also causes an increase in pressure in the stagnation flow region on the suction side of the airfoil. This creates a positive pressure pulse radiating to the upper half-plane. This can be seen in Figs. 16b, c and d. The first positive lobe expands in time. It coalesces with the second lobe and then a pulse is released. On the lower half-plane, a negative pressure pulse is radiated at the same time. However, the negative pressure pulse is produced primarily by the creation of the new vortex pair as shown in Fig. 14b right downstream of the trailing edge. The flow between the two counter-rotating vortex pair is high. This produces a very low pressure region instrumental in causing radiation of a negative pressure pulse. The spread of the wave front in the lower half-plane is shown in Figs. 16c and 16d. The process is clearer by examining a video we have made in slow motion. We would like to emphasize that the positive and negative pulses radiating to the upper and lower half-plane are created by different processes.

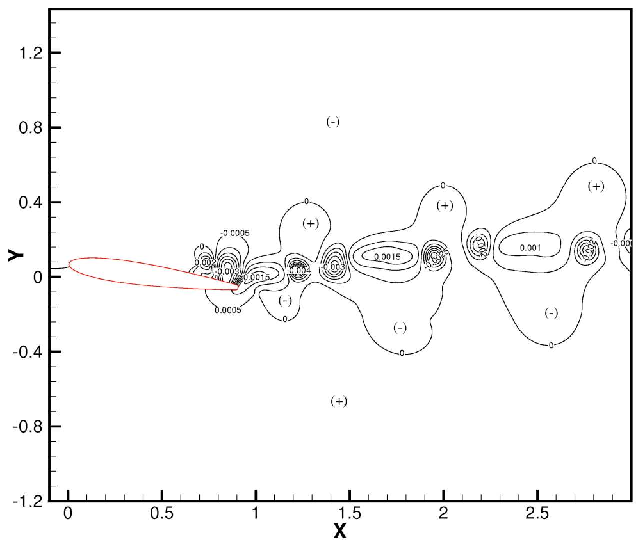

Fig. 16a. The *p'* contour patterns of a NACA0012 airfoil at 8 degrees angle of attack at four instants of time during the first half of a cycle.

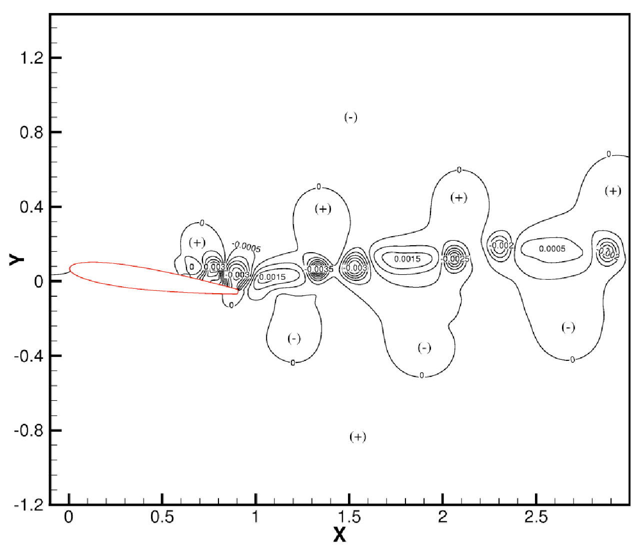

Fig. 16b.

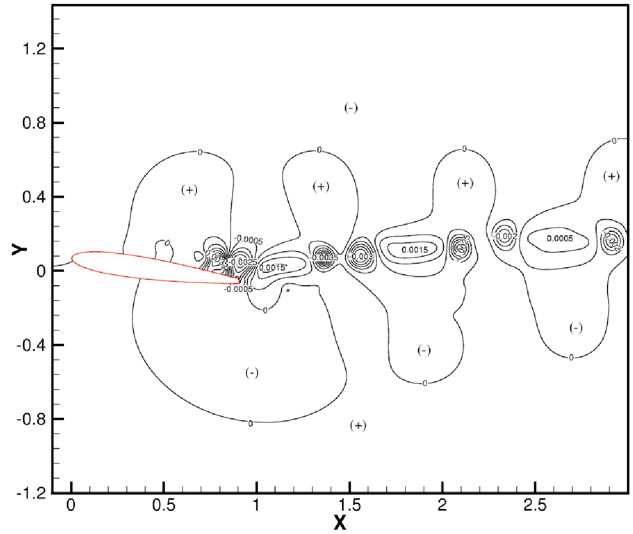

Fig. 16c.

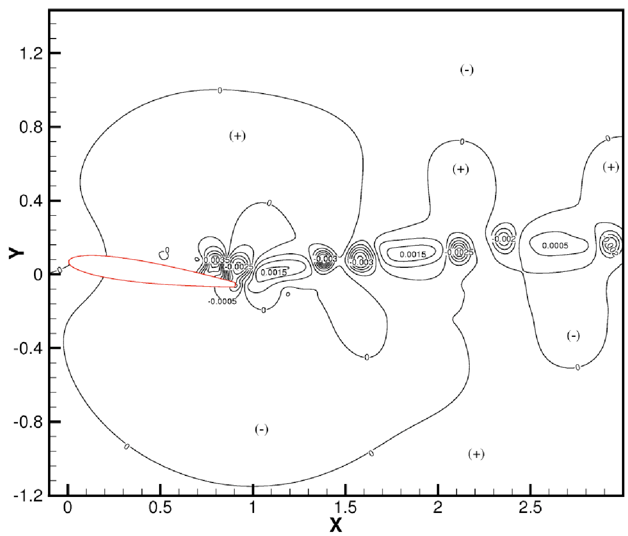

Fig. 16d.

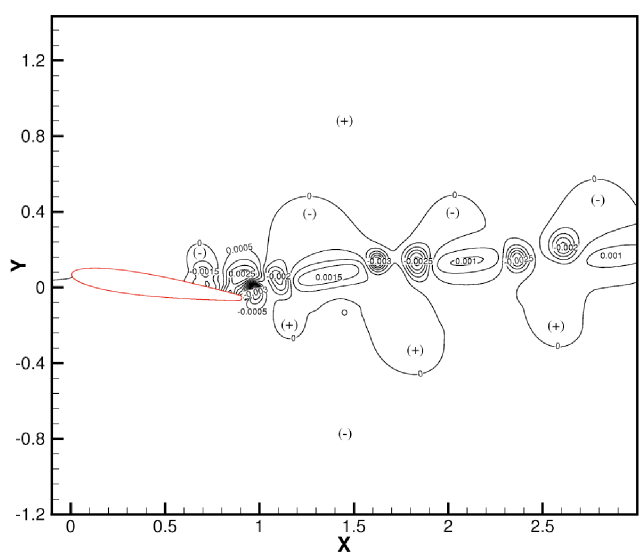

Fig. 17a. The *p'* contour patterns of a NACA0012 airfoil at 8 degrees angle of attack at four instants of time during the second half of a cycle.

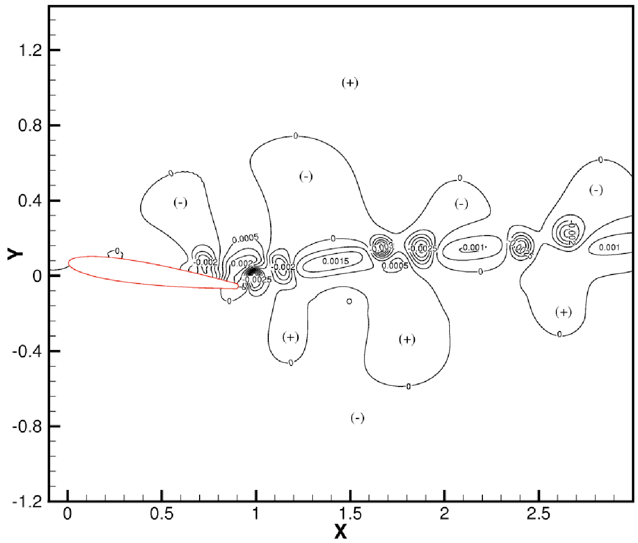

Fig. 17b.

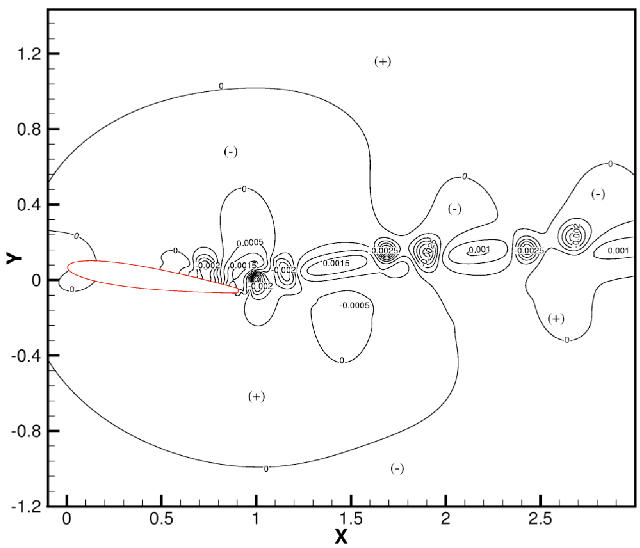

Fig. 17c.

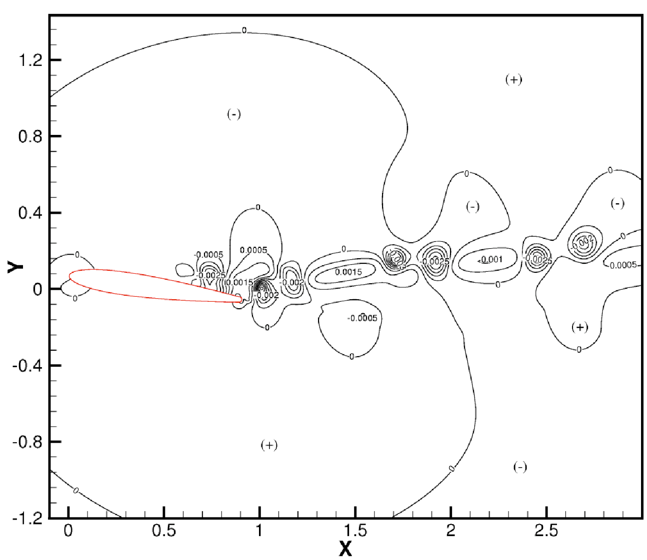

Fig. 17d.

Figures 17a to 17d show the second half of the radiation cycle. Our observation suggests that after a new vortex pair is formed, there is an adjustment of the relative position of the two vortices (see Figs. 14c and 14d). This adjustment of the positions is the primary cause of pressure fluctuation and sound radiation. Again the sound pulse radiating to the top and bottom half of the computational plane are not symmetric.

Figure 18 is the time history of the pressure signal at a point vertically below the trailing edge of the airfoil at a distance of *C*. Figure 19 is the time history of pressure measured at a point vertically above the trailing edge at a distance of *C* from it. The emitted pressure pulses are not symmetric and unalike. They are definitely not sinusoidal. The waveforms of the pressure pulses appear to be a direct consequence that they are produced by a non-localized source and by not so similar processes.

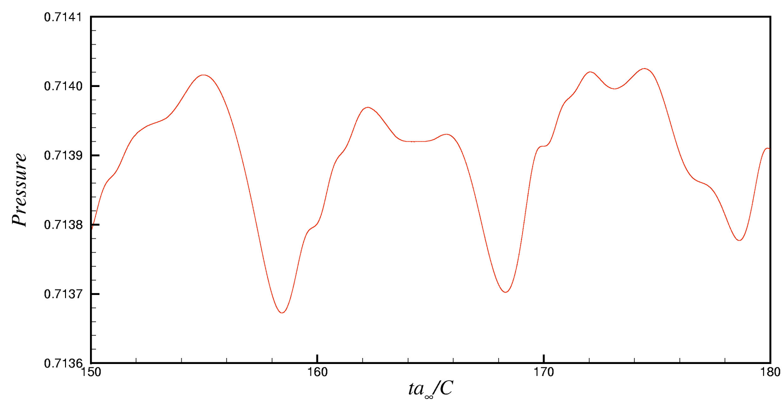

Fig. 18. Pressure time history at a point *C* vertically below the trailing edge of a NACA0012 airfoil at 8 degrees angle of attack.

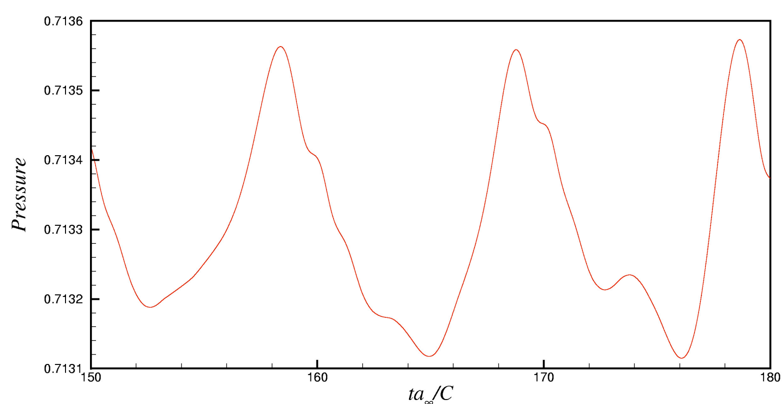

Fig. 19. Pressure time history at a point *C* vertically above the trailing edge of a NACA0012 airfoil at 8 degrees angle of attack.

V. Directivity and Noise Spectra

In this section, the noise spectra and directivity as measured from the numerical simulation are reported. Figure 20 are the relative directivities of the radiated sound from the airfoil at 2°, 6° and 8° angles of attack. There is an over 20 dB difference between the noise intensity at 8° and 2° angle of attack. This is a huge increase of sound confirming a well accepted belief that separated flow is a source of intense noise. We would like to point out that the sound directivity is not that of a point dipole in a uniform flow. Nor is it a baffled dipole; the trailing edge directivity depicted by Ffowcs-Williams and Hall[26]. For low angle of attack, the directivity is nearly perfectly symmetric about the direction of flow. However, at high angle of attack, there is a slight tilt in the directivity pattern.

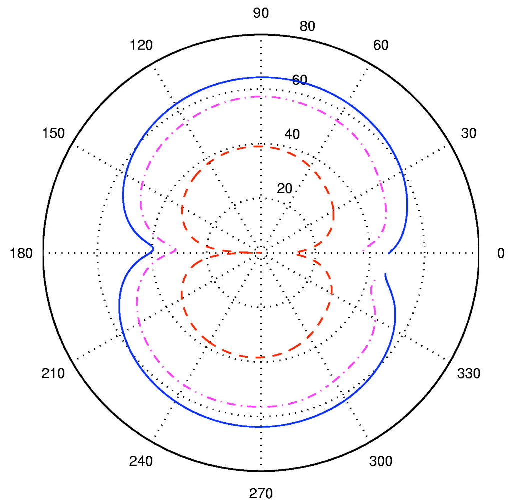

Fig. 20. Directivies of a NACA0012 airfoil in relative dB.
– – – – 2^0 angle of attack, — - — - — 6^0 angle of attack, ——— 8^0 angle of attack.

Figures 21 and 22 are the noise spectra at 2° and 8° angles of attack. At 2° angle of attack, the spectrum consists of mainly a single discrete tone. The pressure wave form is quite sinusoidal. At 8° angle of attack, the spectrum contains many frequencies. In addition to the dominant tone, the first harmonic at about 671 Hz can readily be seen. This is consistent with the experimentally measured noise spectra of Fig. 1, where the fundamental frequency and its first harmonic dominate over the entire spectrum. The higher harmonic can also be identified in Fig. 22. This is not surprising since the waveform of the pressure pulse is far from sinusoidal (see Figs. 18 and 19).

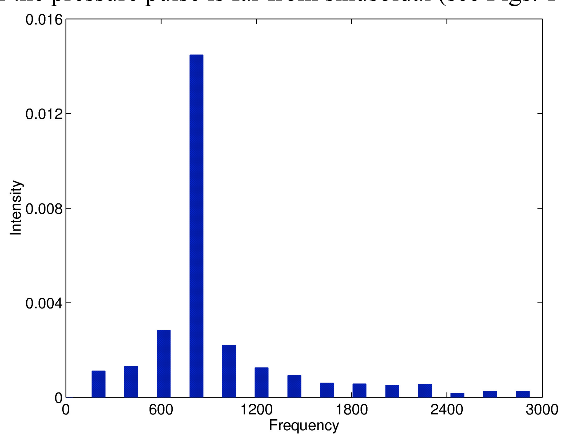

Fig. 21. Noise spectrum of a NACA0012 airfoil at 2 degrees angle of attack.

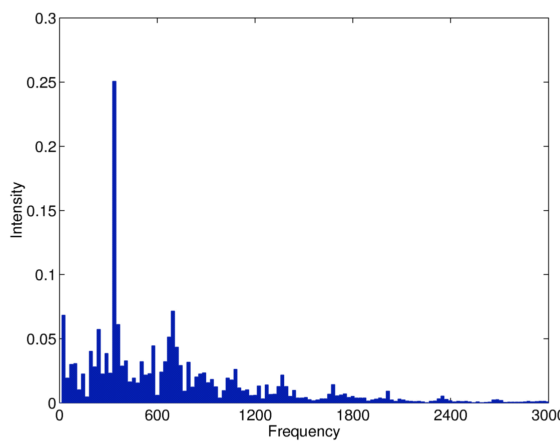

Fig. 22. Noise spectrum of a NACA0012 airfoil at 8 degrees angle of attack.

VI. Conclusions

This work uses Direct Numerical Simulation to investigate the mechanisms of tone generation associated with flow past an airfoil at moderate Reynolds number. This is made possible by the advances in Computational Aeroacoustics methodologies in recent years. Numerical simulation has the important advantage that the full set of space-time data is available to an investigator. The data could then be analyzed and re-analyzed, processed and re-processed in numerous ways to expose the underlying noise generation mechanisms.

In the past, there is a prevalent belief that airfoil tones are produced by very localized dipole located at the trailing edge of the airfoil. Our simulation data indicate that this is not the case for airfoils at moderate Reynolds number. The source of sound is not highly localized and not localized right at the airfoil trailing edge. At high angle of attack, part of the sources is actually located on the suction side of the airfoil. Furthermore, the source of noise responsible for sound radiation to the pressure side and suction side of the airfoil are not the same. This is not anticipated before.

Flow around an airfoil may be classified into four regimes. At low angle of attack, the wake flow is symmetric or very close to symmetric. For this class of flows, the present investigation concludes that the airfoil tones are very much related to the most amplified Kelvin-Helmholtz instability wave of the wake flow. The acoustic energy is very small compared to that of the instability wave. The tone is produced in the near wake as a small by-product of the generation of Kelvin-Helmholtz instability wave. At moderate angle attack, the wake becomes unsymmetric. At high angle of attack, a separation bubble forms just downstream of the airfoil leading edge. In the wake, the flow is dominated by vortices. The wake vortices are shed as vortex pairs. The observation that wake vortices are shed in pairs does not appear to have been reported before. The vortex cores are low pressure regions. But in between vortex pairs the pressure is high. When a new vortex pair is shed, the entire row of wake vortices including the vortices on the suction surface of the airfoil adjust their relative positions to accommodate their presence. This adjustment causes fluctuations in both the high and low pressure regions. These pressure fluctuations immediately lead to acoustic radiation. At still higher angle of attack, there is open separation flow on the back side of the airfoil. In this study only the sound generation mechanisms at low and at high angle of attack are investigated and reported. The cases of moderate angle of attack and open separated flow are to be reported in a subsequent paper.

Acknowledgment

The authors would like to thank Dr. Fang Q. Hu of the Old Dominion University for his assistance in developing the conformal mapping procedure for generating a body fitted grid.

References

[1]Mary, I. and Sagaut, P., "Large Eddy Simulation of Flow Around an Airfoil," AIAA Paper 2001-2559, June 2001.

[2]Cokljat, D. and Liu, F., "DES of Turbulent Flow over an Airfoil at High Incidence," AIAA Paper 2002-0590, January 2002.

[3]Morgan, P.E. and Visbal, M.R., "Large Eddy Simulation of Airfoil Flows," AIAA Paper 2003-0777, January 2003.

[4]Manoha, E., Troff, B. and Sagaut, P. "Trailing-Edge Noise Prediction Using Large-Eddy Simulation and Acoustic Analogy," *AIAA Journal*, Vol. 38, No.4, 2000, pp. 575–583.

[5]Wang, M. and Moin, P., "Computation of Trailing-Edge Flow and Noise Using Large-Eddy Simulation," *AIAA Journal*, Vol. 38, No. 12, 2000, pp. 2201–2209.

[6]Manoha, E., Delahay, C., Sagaut, P., Mary, I., Khelil, S. and Guillen, P., "Numerical Prediction of the Unsteady Flow and Radiated Noise from a 3D Lifting Airfoil," AIAA Paper 2001-2133, May 2001.

[7]Oberai, A.A., Roknaldin, F. and Hughes, T.J.R., "Computation of Trailing-Edge Noise due to Turbulent Flow over an Airfoil," *AIAA Journal*, Vol. 40, No. 11, 2002, pp.2206–2216.

[8]Manoha, E., Herrero, C., Sagaut, P., and Redonnet, S., "Numerical Prediction of Airfoil Aerodynamic Noise," AIAA Paper 2002-2573, June 2002.

[9]Koh, S.R., Chang, K.W. and Moon, Y.J., "Turbulence Trailing Edge Noise at Low Mach Number," AIAA Paper 2005-2974, May 2005.

[10]Marsden, O., Bogey, C. and Bailly, C., "Noise Radiated by a High-Reynolds Number 3-D Airfoil," AIAA Paper 2005-2817, May 2005.

[11]Chang, P.A., Gershfeld, J. and Wang, M., "Towards the Prediction of Vortex Shedding from an Airfoil using LES," AIAA Paper 2003-3109, May 2003.

[12]Lummer, M., Delfs, J.W. and Lauke, T., "Simulation of the Influence of Trailing Edge Shape on Airfoil Sound Generation," AIAA Paper 2003-3109, May 2003.

[13]Guidati, G., Ostertag, J. and Wagner, S., "Prediction and Reduction of Wind Turbine Noise — An Overview of Research Activities in Europe," AIAA Paper 2000-0042, January 2000.

[14]Moriaty, P.J., Guidati, G. and Migliore, P., "Recent Improvement of a Semi-Empirical Aeroacoustic Prediction Code for Wind Turbines," AIAA Paper 2004-3041, May 2004.

[15]Moriaty, P.J., Guidati, G. and Migliore, P., "Prediction of Turbulent Inflow and Trailing-Edge Noise for Wind Turbines," AIAA Paper 2005-2881, May 2005.

[16]Brooks, T., Pope, D. and Marcolini, M., "Airfoil Self-Noise Prediction," NASA RP-1218, NASA 1989.

[17]Roger, M. and Moreau, S. "Broadband Self-Noise from Loaded Fan Blades," *AIAA Journal*, Vol. 42, No. 3, 2004, pp. 536–544.

[18]Moreau, S. and Roger, M., "Effect of Angle of Attack and Airfoil Shape on Turbulence-Interaction Noise," AIAA Paper 2005-2973, May 2005.

[19]Shannon, D.W., Morris, S.C. and Mueller, T.J., "Trailing Edge Flow Physics and Acoustics," AIAA Paper 2005-2957, May 2005.

[20]Oerlemans, S., "Wind Tunnel Aeroacoustic Tests of Six Airfoils for Use on Small Wind Turbines," National Aerospace Laboratory, Emmeloord, the Netherlands, NREL SR-500-34470, 2003.

[21]Hansen, A.C. and Butterfield, C.P., "Aerodynamics of Horizontal-Axis Wind Turbines," *Annual Review of Fluid Mechanics*, Vol. 24, 1993, pp. 115–144.

[22]Tam, C.K.W. and Webb, J.C., "Dispersion-Relation-Preserving Scheme for Computational Acoustics," *Journal of Computational Physics*, Vol. 107, 1993, pp. 262–281.

[23]Tam, C.K.W. and Kurbatskii, K.A., "Multi-Size-Mesh Multi-Time-Step Dispersion-Relation-Preserving Scheme for Multiple Scales Aeroacoustics Problems," *International Journal of Computational Fluid Dynamics*, Vol. 17, No. 2, 2003, pp. 119–132.

[24]Tam, C.K.W. and Hu, F.Q., "An Optimized Multi-Dimensional Interpolation Scheme for Computational Aeroacoustics Applications Using Overset Grids," AIAA Paper 2004-2812, May 2004.

[25]Tam, C.K.W., Webb, J.C. and Dong, A., "A Study of the Short Wave Component in Computational Acoustics," *Journal of Computational Acoustics*, Vol. 1, No. 1, 1993, pp. 1–30.

[26]Ffowcs Williams, J.E. and Hall, L.H., "Aerodynamic Sound Generation by Turbulent Flow in the Vicinity of a Scattering Half-Plane," *Journal of Fluid Mechanics*, Vol. 40, No. 4, 1970, pp. 657–670.